The S-layer homology domains of *Paenibacillus alvei* surface protein SpaA bind to cell wall polysaccharide through the terminal monosaccharide residue

Max S. G. Legg[1], Fiona F. Hager-Mair[2], Simon Krauter[3], Susannah M. L. Gagnon[1], Arturo Lòpez-Guzmán[2], Charlie Lim[3], Markus Blaukopf[3], Paul Kosma[3], Christina Schäffer[2], and Stephen V. Evans[1],*

From the [1]Department of Biochemistry & Microbiology, University of Victoria, Victoria, British Columbia, Canada; [2]Department of NanoBiotechnology, NanoGlycobiology Unit, and [3]Department of Chemistry, Institute of Organic Chemistry, Universität für Bodenkultur Wien, Vienna, Austria

Edited by Gerald Hart

Self-assembling (glyco)protein surface layers (S-layers) are ubiquitous prokaryotic cell-surface structures involved in structural maintenance, nutrient diffusion, host adhesion, virulence, and other processes, which makes them appealing targets for therapeutics and biotechnological applications as biosensors or drug delivery systems. However, unlocking this potential requires expanding our understanding of S-layer properties, especially the details of surface-attachment. S-layers of Gram-positive bacteria often are attached through the interaction of S-layer homology (SLH) domain trimers with peptidoglycan-linked secondary cell wall polymers (SCWPs). Cocrystal structures of the SLH domain trimer from the *Paenibacillus alvei* S-layer protein SpaA (SpaA$_{SLH}$) with synthetic, terminal SCWP disaccharide and trisaccharide analogs, together with isothermal titration calorimetry binding analyses, reveal that while SpaA$_{SLH}$ accommodates longer biologically relevant SCWP ligands within both its primary (G2) and secondary (G1) binding sites, the terminal pyruvylated ManNAc moiety serves as the nearly exclusive SCWP anchoring point. Binding is accompanied by displacement of a flexible loop adjacent to the receptor site that enhances the complementarity between protein and ligand, including electrostatic complementarity with the terminal pyruvate moiety. Remarkably, binding of the pyruvylated monosaccharide SCWP fragment alone is sufficient to cause rearrangement of the receptor-binding sites in a manner necessary to accommodate longer SCWP fragments. The observation of multiple conformations in longer oligosaccharides bound to the protein, together with the demonstrated functionality of two of the three SCWP receptor-binding sites, reveals how the SpaA$_{SLH}$-SCWP interaction has evolved to accommodate longer SCWP ligands and alleviate the strain inherent to bacterial S-layer adhesion during growth and division.

Prokaryotic surface layers (S-layers) are composed of (glyco) protein subunits that self-assemble into two-dimensional paracrystalline lattices attached to the exterior of the cell envelope (Fig. 1) (1–7). As one of the most abundant prokaryotic protein systems, S-layer functions are varied and involve biological processes such as cell shaping, structural maintenance, nutrient diffusion, host adhesion, and virulence, among others (4, 8–11), and provide an excellent opportunity for studying fundamentals of protein transport, structure, and assembly. Together with their high surface accessibility, these features make S-layers appealing therapeutic targets with significant biotechnological potential as both biosensors and as drug delivery systems (4, 12–19). Expanding our understanding of S-layer surface-attachment represents an essential step toward exploiting this potential.

To maintain S-layer function while coping with the structural demands of cellular growth and division (4), prokaryotes have evolved covalent and noncovalent S-layer cell-matrix anchoring mechanisms that rely on high affinity but nevertheless flexible attachments to cell wall structures. While S-layers are found in archaea (4, 20, 21) and Gram-negative bacteria (9, 22, 23), only in Gram-positive bacteria are they anchored to the cell wall *via* evolutionarily conserved S-layer homology (SLH) domains (4, 9, 24–26), which generally occur as triplicate repeats (SLH1, SLH2, and SLH3) located at the protein C-terminus or immediately after the N-terminal signal peptide (4, 9, 24–26). SLH domains have been shown to bind noncovalently neutral or anionic polysaccharides called non-classical secondary cell wall polymers (SCWPs) that are themselves covalently linked to the muramic acid residues of peptidoglycan (Fig. 1) (11).

Recently published structures of the SLH-domain trimers from the S-layer proteins SpaA (*Paenibacillus alvei*) (27) and Sap (*Bacillus anthracis*) (28, 29) show overall threefold symmetry, where the ~55 residue repeats each consist of two α-helices connected by an extended loop (27–29). The C-terminal helix from each SLH repeat contributes to a three-helix core bundle parallel to the threefold symmetry axis, while the corresponding N-terminal helix is rotated ~90° from the threefold axis to form three alternating lobes and grooves (27, 28). The N-terminus of each core helix for *P. alvei* SpaA contributes a conserved "TRAE" motif toward these binding grooves, where TRAE of SLH1, TVEE of SLH2, and TRAQ of

* For correspondence: Stephen V. Evans, svevans@uvic.ca.
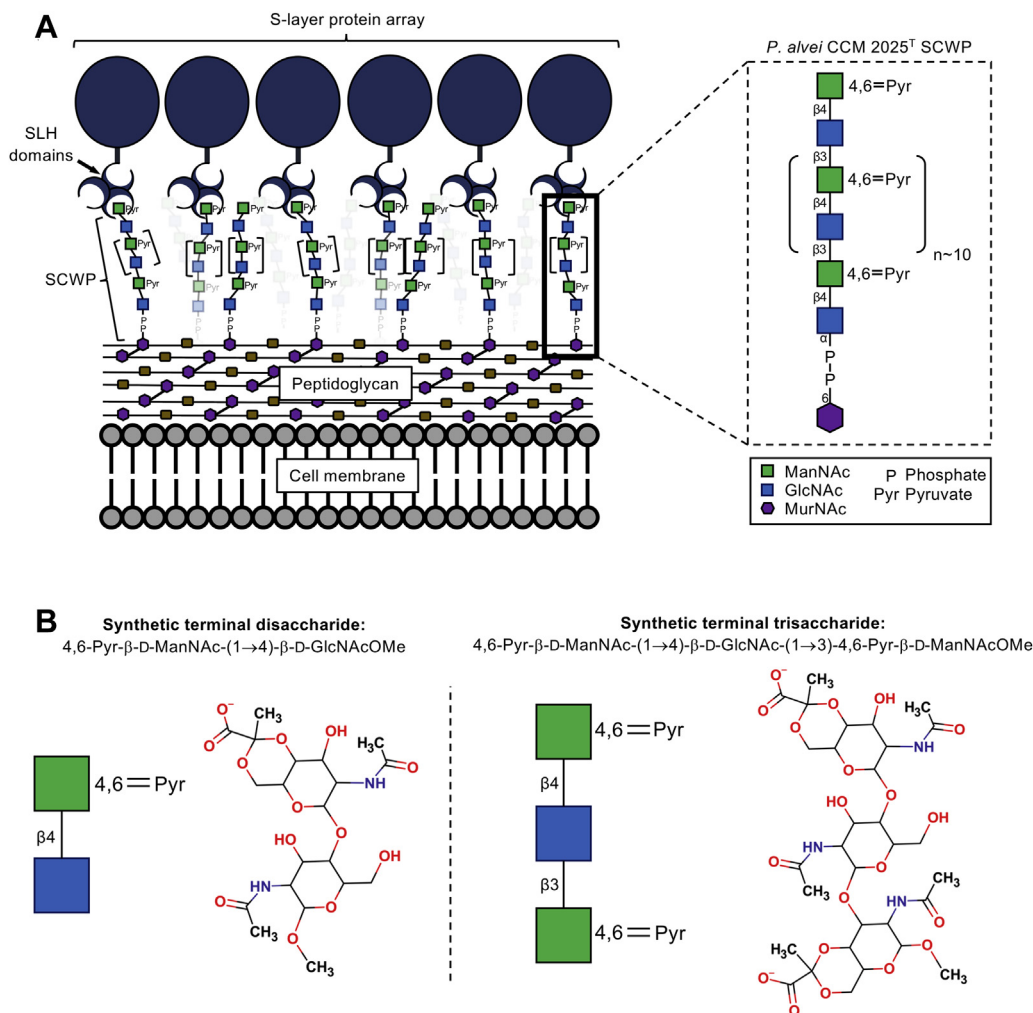
Figure 1. The cell surface of many prokaryotes is coated in a surface layer (S-layer) consisting of one or more (glyco)proteins arranged in a repeating two-dimensional array. *A*, schematic diagram of S-layer protein binding on Gram-positive bacteria mediated *via* specialized S-layer homology (SLH) domains that recognize and bind peptidoglycan-linked secondary cell wall polymers (SCWPs), with the inset showing the structure of the SCWP from *P. alvei* CCM 2051[T] (11, 27, 30); and (*B*) the synthetic ligand analogs used in this study corresponding to the terminal disaccharide and trisaccharide units of the *P. alvei* CCM 2051[T] SCWP ligand.

SLH3 are primarily situated within grooves 1 (G1), 2 (G2), and 3 (G3), respectively (27, 28). The side chains of the arginine residues of the TRAE (SLH1) and TRAQ (SLH3) motif extend through the hydrophobic core to emerge at the base of the neighboring grooves G2 and G1, respectively, where their positively charged guanidino groups are positioned to complement the negatively charged SCWP ligands.

P. alvei CCM 2051[T] (henceforth *P. alvei*) SCWP is composed of 11 →3)-4,6-Pyr-β-D-Man*p*NAc-(1→4)-β-D-Glc*p*NAc-(1→ repeats (30). The binding of a synthetic, terminal 4,6-Pyr-β-D-ManNAcOMe SCWP monosaccharide analog to an SLH domain has been shown to induce a remarkable structural rearrangement involving an ~180° phi angle backbone flip of a conserved glycine residue (consensus sequence SLH-Gly29) fundamental to the receptor site's ability to bind ligand, including accommodation of the negative charge of the terminal pyruvate moiety (27). Together with enzymatic and biochemical analyses, these structural findings

confirm that, for SpaA, Sap, and other Gram-positive S-layer proteins, SLH-mediated SCWP anchoring is reliant on a negatively charged ketal-pyruvate moiety located on the terminal sugar residue of the SCWP (27, 29–33).

P. alvei SpaA$_{SLH}$ monosaccharide-bound structures identified separate SLH-domain binding sites in G2 and G1 (27). Specifically, wild-type SpaA$_{SLH}$ protein was first observed with ligand bound in G2, and upon inactivation of binding in G2 through a mutation of its conserved glycine residue to alanine (G109A), a remarkable conformational shift was observed where the mutant construct instead utilized G1 for binding with a concomitant tenfold decrease of the associated ITC monosaccharide binding affinity (27). The double mutation of conserved glycine residues in G1 and G2 to alanine (G46A/G109A) abolished SpaA$_{SLH}$'s ligand-binding ability (27). Together, these observations show that monosaccharide SCWP binding is likely centered about G2, with G1 serving as the alternate site for SCWP binding (27).

Significantly, the ability of SpaA$_{SLH}$ to accommodate monosaccharide binding in G2 or G1 suggests a biological mechanism for the relief of S-layer strain encountered during processes of cellular growth and division (27), where the transfer of SCWP interactions between SLH-domain binding sites could facilitate S-layer rearrangement and expansion without disrupting the overall confluence of the S-layer protein lattice. To date, however, the analysis of this novel binding site switching mechanism has been limited to the terminal monosaccharide 4,6-Pyr-β-ᴅ-ManNAcOMe and the internal repeat disaccharide β-ᴅ-GlcNAc-(1→3)-4,6-Pyr-β-ᴅ-ManNAcOMe SCWP ligand analogs (27), leaving open the role of the subsequent SCWP sugar residues in binding, as well as whether the primary G2 and secondary G1 sites can accommodate longer ligands that better approximate SCWP at the surface of *P. alvei*. To address this, here, we characterize the details of the SpaA$_{SLH}$-SCWP interaction using thermodynamic isothermal titration calorimetry (ITC) analysis of disaccharide and trisaccharide binding and through the determination of the cocrystal structures of SpaA$_{SLH}$, and single (SpaA$_{SLH}$/G109A) and the corresponding double (SpaA$_{SLH}$/G46A/G109A) mutants in complex with synthetic terminal disaccharide and trisaccharide analogs of the *P. alvei* SCWP ligand.

Results

Binding parameters of SpaA$_{SLH}$ and disaccharide and trisaccharide SCWP analog

ITC was used to assess the ability of SpaA$_{SLH}$, SpaA$_{SLH}$/G109A, and SpaA$_{SLH}$G46A/G109A to bind the terminal 4,6-Pyr-β-ᴅ-ManNAc-(1→4)-β-ᴅ-GlcNAcOMe disaccharide analog and the 4,6-Pyr-β-ᴅ-ManNAc-(1→4)-β-ᴅ-GlcNAc-(1→3)-4,6-Pyr-β-ᴅ-ManNAcOMe trisaccharide analog in solution (Table 1). The disaccharide binds with 1:1-stoichiometry and an apparent dissociation constant (K_D) of 64 nM at 20 °C for the wild-type protein SpaA$_{SLH}$ and of 288 nM at 20 °C for the SpaA$_{SLH}$/G109A mutant (Table 1). The binding affinity toward the disaccharide was determined to be slightly lower compared with the monosaccharide (27) (Table 1) while interestingly, the trisaccharide analog shows a slightly lower K_D (4.7 nM at 20 °C) implicating a slightly

higher binding affinity toward the wild-type protein SpaA$_{SLH}$. With the G109A single mutant, the K_D drops 55-fold (260 nM at 20 °C) compared with trisaccharide binding data for the wild-type protein (27). Despite a similar Gibbs free energy (ΔG), the entropic contribution is comparably stronger with both trisaccharide and disaccharide compared with the monosaccharide (Table 1) resulting in an overall lower enthalpic contribution. For visualization, a comparison of the binding energies is shown in Fig. S1; and binding isotherms are shown in Fig. S2. The binding data of the di- and trisaccharide support a favorable hydrogen bond formation and hydrophobic interaction, while the binding data of the monosaccharide (27) support a good hydrogen bonding with unfavorable conformational change. With neither of the synthetic SCWP analogs, binding is observed with the SpaA$_{SLH}$G46A/G109A double mutant (Table 1).

Structures of ligand-bound SpaA$_{SLH}$

Data collection and refinement statistics for ligand-bound SpaA$_{SLH}$, SpaA$_{SLH}$/G109A, and SpaA$_{SLH}$G46A/G109A structures are summarized in Table 2. All X-ray diffraction data were collected to 2.06 to 1.70 Å resolution (Table 2) using a Dectris Pilatus 200K detector coupled to a Micromax-007 HF X-ray generator (Rigaku), with crystals flash frozen at 100K using an Oxford Cryosystems Cryostream Unit (800 series). Structure solutions were determined using molecular replacement (PHASER from the CCP4 suite (34)), with iterative refinements (REFMAC5 from the CCP4 suite (34)) yielding final R$_{work}$, R$_{free}$, and average *B* factor values in the ranges of 17.8 to 20.5%, 19.5 to 24.0%, and 17.1 to 26.2 Å^2, respectively (Table 2). In the disaccharide-bound SpaA$_{SLH}$ (with residues 28–197 modeled), SpaA$_{SLH}$/G109A (with molecule A: residues 28–192 modeled, and molecule B: residues 28–191 modeled), SpaA$_{SLH}$G46A/G109A (with residues 28–192 modeled), and trisaccharide-bound SpaA$_{SLH}$ (with residues 28–197 modeled) structures, nearly all residues display unambiguous electron density, while the first modeled residue (Ala28) in each structure, and the last few modeled residues from the disaccharide-bound SpaA$_{SLH}$ (residues 194–197), SpaA$_{SLH}$/G109A (molecule A: residue 192; molecule B: residues 189–191), SpaA$_{SLH}$G46A/G109A (residues 191–192), and trisaccharide-bound SpaA$_{SLH}$ (residues

Table 1

ITC analysis of SpaA$_{SLH}$ binding of the 4,6-Pyr-β-ᴅ-ManNAc-(1→4)-β-ᴅ-GlcNAcOMe disaccharide and the 4,6-Pyr-β-ᴅ-ManNAc-(1→4)-β-ᴅ-GlcNAc-(1→3)-4,6-Pyr-β-ᴅ-ManNAcOMe trisaccharide ligands

Ligand bound to SpaA$_{SLH}$ variant	Temperature (°C)	−TΔS (kJ/mol)	ΔH (kJ/mol)	ΔG (kJ/mol)	Stoichiometry	K_A (M^{-1})	K_D (nM)
Trisaccharide-binding data							
SpaA$_{SLH}$	20	−18.70 ± 5.57	−27.14 ± 3.29	−45.84 ± 2.29	1.16 ± 0.10	2.14 × 10^8 ± 1.46	4.7
SpaA$_{SLH}$/G109A	20	−15.99 ± 1.00	−20.92 ± 0.57	−36.91 ± 0.47	1.44 ± 0.25	3.84 × 10^6 ± 0.68	260
SpaA$_{SLH}$/G46A/G109A	20	No binding					
Disaccharide-binding data							
SpaA$_{SLH}$	20	−9.95 ± 2.08	−30.36 ± 1.64	−40.31 ± 0.65	1.20 ± 0.16	1.56 × 10^7 ± 0.37	64
SpaA$_{SLH}$/G109A	20	−15.74 ± 1.35	−20.95 ± 1.51	−36.70 ± 0.20	1.30 ± 0.19	3.47 × 10^6 ± 0.29	288
SpaA$_{SLH}$/G46A/G109A	20	No binding					
Previously published (27) monosaccharide-binding data							
SpaA$_{SLH}$	20	45.74 ± 16.01	−87.85 ± 15.62	−42.10 ± 0.65	0.91 ± 0.04	3.48 × 10^7 ± 0.36	29
SpaA$_{SLH}$/G109A	20	13.33 ± 7.0	−50.64 ± 7.29	−37.31 ± 0.33	0.92 ± 0.04	4.48 × 10^6 ± 0.62	226
SpaA$_{SLH}$/G46A/G109A	20	No binding					

For comparison, the published ITC data for 4,6-Pyr-β-ᴅ-ManNAcOMe monosaccharide binding (27) is included.

Table 2
Data collection and refinement statistics for di- and trisaccharide-bound SpaA_{SLH} wild-type and the disaccharide-bound single mutant and double mutant

Protein	SpaA_{SLH}	SpaA_{SLH}	SpaA_{SLH}/G109A	SpaA_{SLH}/G46A/G109A
Ligand	Disaccharide[a]	Trisaccharide[b]	Disaccharide[a]	Disaccharide[a]
PDB code	7SV3	7SV4	7SV5	7SV6
Data collection				
Space group	P2_12_12_1	P2_12_12_1	C2	P2_12_12_1
Resolution (Å)	20.00–1.70 (1.76–1.70)	20.00–2.06 (2.13–2.06)	20.00–1.72 (1.78–1.72)	20.00–1.85 (1.92–1.85)
Cell dimensions				
a (Å)	34.65	34.69	111.85	33.30
b (Å)	67.92	67.30	45.32	65.61
c (Å)	72.91	72.75	87.49	72.29
α (°)	90	90	90	90
β (°)	90	90	129.47	90
γ (°)	90	90	90	90
Z	4	4	8	4
R_{sym}	0.145 (0.773)	0.143 (0.591)	0.071 (0.539)	0.099 (0.540)
R_{pim}	0.048 (0.369)	0.043 (0.295)	0.029 (0.301)	0.053 (0.345)
$CC_{1/2}$	(0.774)	(0.137)	(0.699)	(0.795)
I/σ(I)	8.4 (2.0)	7.6 (2.3)	11.1 (1.9)	9.5 (2.1)
Completeness (%)	100.0 (99.9)	98.4 (90.1)	90.3 (82.6)	98.2 (99.3)
Redundancy	7.9 (5.2)	10.2 (3.3)	6.7 (3.6)	4.3 (3.2)
Unique reflections	19,791	11,130	32,683	13,823
Refinement				
Resolution (Å)	20.00–1.70	20.00–2.06	20.00–1.72	20.00–1.85
No. reflections	18,483	10,409	30,968	13,083
R_{work} (%)	18.4	20.5	17.8	18.6
R_{free} (%)	21.3	24.0	19.5	21.7
No. atoms				
Protein	1311	1290	2520	1281
Ligand(s)	35[a]	66[b,c]	82[a,c]	35[a]
Water	242	137	303	112
B factors (Å²)				
Protein	15.1	25.0	21.2	22.4
Ligand	18.0	34.6	19.5	37.1
Water	27.5	32.6	31.6	31.6
Average	17.1	26.2	22.2	23.5
Ramachandran				
Favored (%)	98.2	98.8	98.5	98.8
Allowed (%)	1.8	1.2	1.5	1.2
Disallowed (%)	0	0	0	0
r.m.s. bonds (Å)	0.0039	0.0031	0.0034	0.0040
r.m.s. angles (°)	1.25	1.23	1.21	1.23

[a] Disaccharide = 4,6-Pyr-β-D-ManNAc-(1→4)-β-D-GlcNAcOMe.
[b] Trisaccharide = 4,6-Pyr-β-D-ManNAc-(1→4)-β-D-GlcNAc-(1→3)-4,6-Pyr-β-D-ManNAcOMe.
[c] Glycerol = $C_3H_8O_3$.

196–197) structures, each, display partial main chain and side-chain electron density, which is consistent with previous SpaA_{SLH} structures (27). Further, the di- and trisaccharide analogs bound by wild-type SpaA_{SLH} (Fig. 2, *A* and *B*), as well as the disaccharide analog bound by the SpaA_{SLH}G109A single mutant (Fig. 2*C*) and SpaA_{SLH}G46A/G109A double mutant (Fig. 2*D*) all display unambiguous electron density for the entire ligand.

Cocrystallization with SCWP terminal disaccharide and trisaccharide

To investigate the molecular details of SpaA_{SLH} SCWP binding, the synthesized *P. alvei* SCWP terminal disaccharide analog 4,6-Pyr-β-D-ManNAc-(1→4)-β-D-GlcNAcOMe (35) (Fig. 1*B*) was cocrystallized with wild-type SpaA_{SLH}. The structure reveals unambiguous electron density for the entire disaccharide bound in G2 (Fig. 2*A*), where the terminal ManNAc residue binds in the same manner to that of the published structure of monosaccharide-bound SpaA_{SLH} (27) within a deep, narrow positively charged pocket lined by residues contributed by all three SLH domains. The pyruvate moiety forms a salt-bridge interaction with TRAE residue Arg61 from SLH1 (corresponding to SLH-Arg43) as well as a hydrogen bond to the backbone amide of Gly109 from SLH2 (corresponding to SLH-Gly29), while the terminal ManNAc ring forms a stacking interaction with Trp151 from SLH3 (corresponding to SLH-Trp13) (Fig. 2*A*). The disaccharide β(1→4) linkage extends past the edges of the binding pocket, which forces the GlcNAc residue to project out from the binding site without forming direct hydrogen bond contacts with SpaA_{SLH} surface residues, although it does interact through an ordered network of bridging water molecules to surface residues Lys110, Glu127, and Trp151 (Fig. 3*A*).

The *P. alvei* SCWP terminal trisaccharide analog 4,6-Pyr-β-D-ManNAc-(1→4)-β-D-GlcNAc-(1→3)-4,6-Pyr-β-D-ManNAcOMe (Fig. 1*B*) was also synthesized (see Supporting information) and cocrystallized with wild-type SpaA_{SLH}. The resultant cocrystal structure reveals clear electron density for the entire trisaccharide ligand bound to the G2 pocket (Fig. 2*B*). However, while the terminal, pyruvylated ManNAc residue binds in the same manner as observed for the disaccharide (above) and monosaccharide (27) SpaA_{SLH} structures (Fig. 3*B*), the GlcNAc residue adopts a rotated conformation
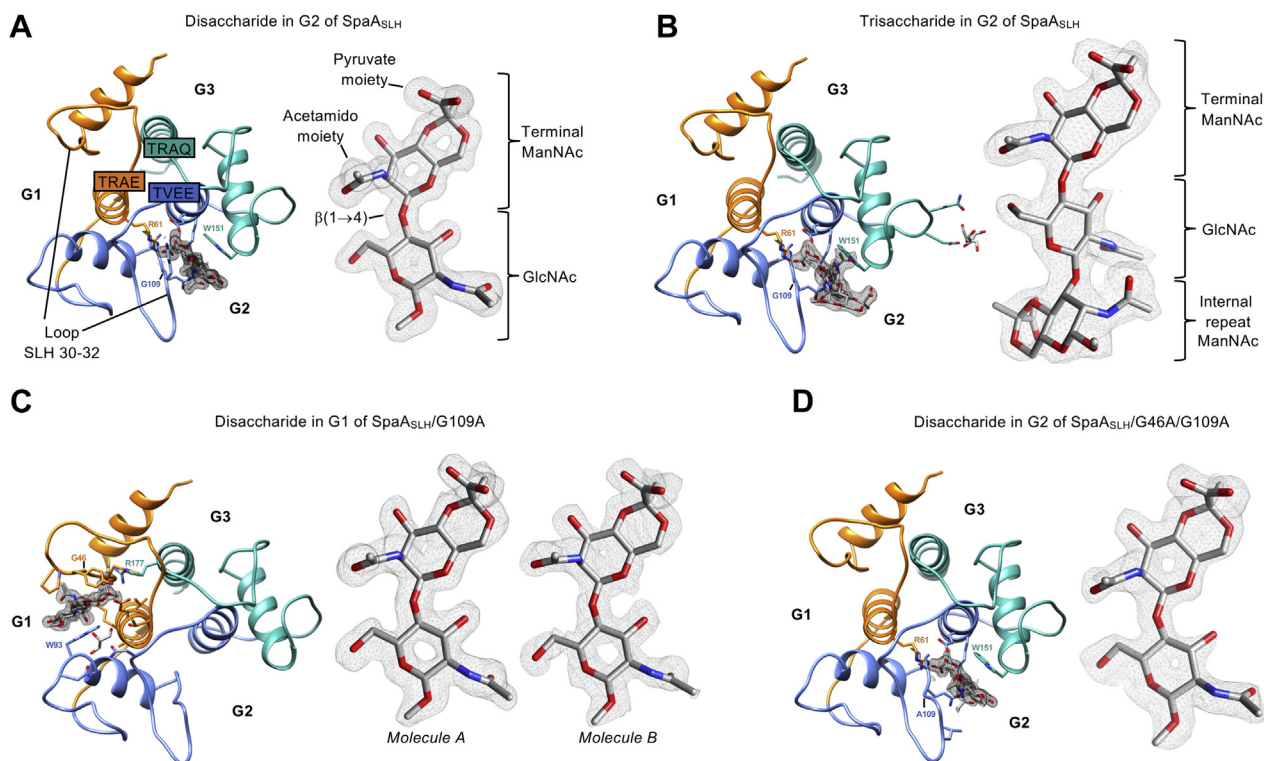
Figure 2. Ribbon models for each SpaA$_{SLH}$ co-crystal structure in Table 2. 2F$_o$-F$_c$ electron density maps contoured to 1σ shown for the corresponding model of bound ligand for (*A*) disaccharide-bound SpaA$_{SLH}$; (*B*) trisaccharide-bound SpaA$_{SLH}$; (*C*) disaccharide-bound SpaA$_{SLH}$/G109A with ligands shown from both molecules of the asymmetric unit of the co-crystal structure; and (*D*) disaccharide-bound SpaA$_{SLH}$/G46A/G109A double mutant. Grooves 1, 2, and 3 are indicated on each structure as G1, G2, and G3, respectively. SLH1 *orange*, SLH2 *blue*, and SLH3 *aquamarine*. Ligand atoms are colored by element with oxygen *red*, nitrogen *blue*, and carbon *white*. 2F$_o$-F$_c$ electron density maps are depicted as *gray mesh*.

where the acetamido moiety is displaced 4.5 Å toward the opposite face of the binding pocket, to form a single hydrogen bond contact with the protein surface and bridging water molecule contacts with Lys110, Glu127, and Thr149 (Fig. 3*B*). This results in the GlcNAc O3 hydroxyl being shifted by 2.1 Å with respect to the disaccharide, to form a hydrogen bond and water bridge to Trp151 and Glu127, respectively (Fig. 3*B*). In trisaccharide-bound SpaA$_{SLH}$, the internal-repeat ManNAc residue forms a 3.2 Å hydrogen bond to the GlcNAc acetamido moiety and bridging water interactions to surface residues Lys110 and Asp150 (Fig. 3*B*).

The terminal disaccharide analog also cocrystallized in G2 of SpaA$_{SLH}$/G46A/G109A, with the overall protein structure exhibiting a high degree of structural homology to disaccharide-bound SpaA$_{SLH}$ (with an overlap Cα rmsd of 0.44 Å), while displaying unambiguous electron density for the entire ligand (Fig. 2*D*).

The terminal disaccharide analog was also cocrystallized with the SpaA$_{SLH}$/G109A single mutant designed to destabilize ligand binding in G2. The structure displays unambiguous electron density for the entire disaccharide ligand within G1 (Fig. 2*C*), where the terminal ManNAc ring of the disaccharide sits deep within the G1 pocket lined by conserved residues Arg177 of SLH3 (corresponding to conserved residue SLH-Arg43), Trp93 of SLH2 (corresponding to the conserved residue SLH-Trp13), and Gly46 (corresponding to conserved residue SLH-Gly29). The disaccharide's β(1→4) linkage does

not extend entirely past the mouth of the G1 pocket, and the lower portion of the GlcNAc sugar residue remains partially obscured by residues Pro48 and Trp93 of SLH2 (Fig. 3*C*). The extended GlcNAc residue does not form any direct hydrogen bonds with the protein, but derives partial stability from hydrophobic contacts with Pro48 and Trp93 (Fig. 3*C*). The GlcNAc O3 hydroxyl simultaneously forms a water-bridge with Glu63, while coordinating the ManNAc O5 hydroxyl and GlcNAc *N*-acetyl nitrogen (Fig. 3*C*). The GlcNAc acetamido substituent forms a hydrogen bond with a surface-associated glycerol molecule (Fig. 3*C*).

GlcNAc sugar occupancy in disaccharide-bound SpaASLH

In the cocrystal structure of disaccharide-bound SpaA$_{SLH}$, unexplained electron density was observed in G2 near the GlcNAc sugar moiety of the ligand, which could be explained by the GlcNAc sugar residue being disordered over two conformations (Fig. 3*D*), with the second conformation (Conformation 2) lying in the difference density. The occupancy of the primary GlcNAc conformation (Conformation 1) was adjusted to 50% to yield temperature factors comparable with those of surrounding protein and ligand atoms, ranging between 10.00 and 19.00.

In conformation 1, the acetamido and O3 hydroxyl groups are positioned nearest the region of the binding pocket where residue Lys110 is located (Fig. 3*A*). In conformation 2, the
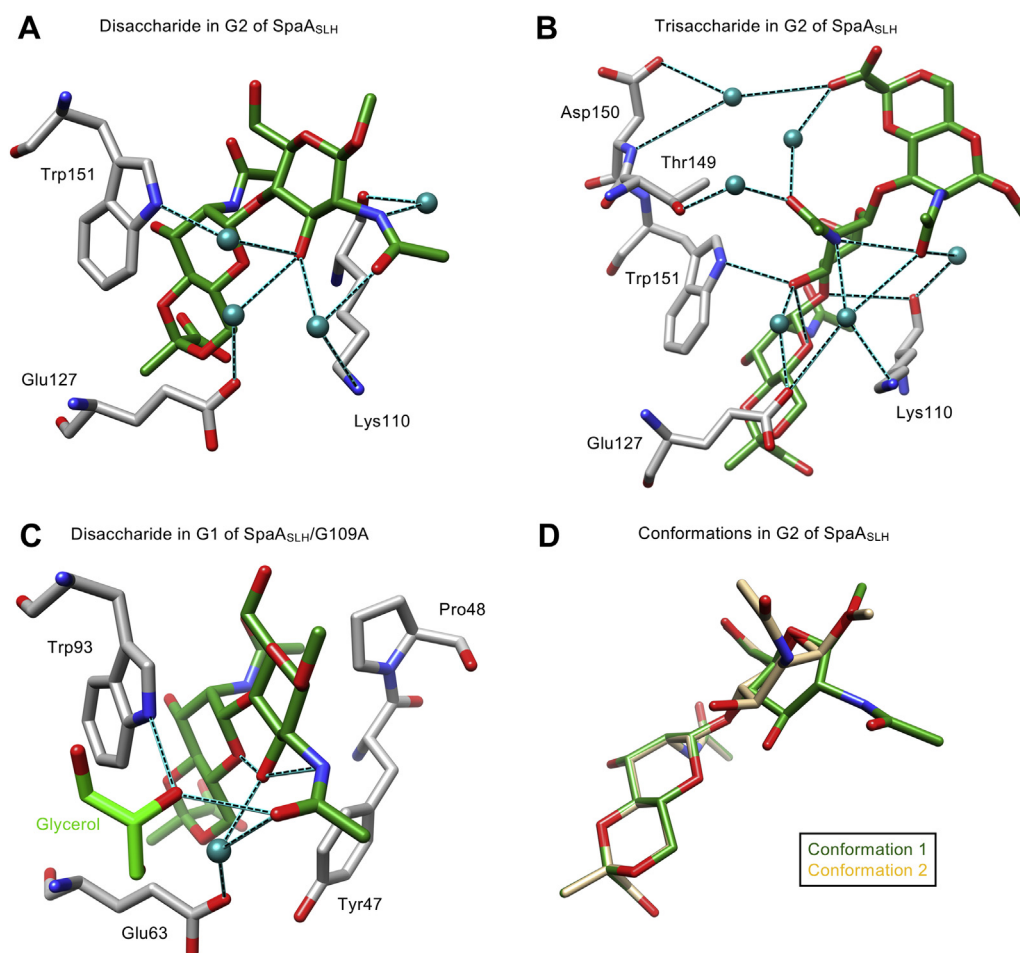
Figure 3. Only the terminal monosaccharide of the di- and trisaccharide ligands forms significant direct contacts with the SpaA_{SLH} protein, with the internal saccharide residues forming mainly bridging water contacts. *A*, the synthetic terminal disaccharide analog binds to G2 of SpaA_{SLH}, with the GlcNAc residue forming no direct contact to the protein. *B*, the synthetic terminal trisaccharide analog binds to G2 of SpaA_{SLH}, with the GlcNAc residue forming a single hydrogen bond interaction with the protein. *C*, the synthetic terminal disaccharide analog binds to G1 of the single mutant with the terminal ManNAc again forming the only direct interactions with the protein. *D*, the GlcNAc residue bound to G2 of the wild-type SpaA_{SLH} is disordered over two conformations, with the second conformation corresponding to the GlcNAc orientation observed in trisaccharide-bound SpaA_{SLH} structure. Water molecules are depicted as *light green spheres*, while atoms are colored by element with oxygen *red*, nitrogen *blue*, protein carbon *white*, and ligand carbon *green* (or tan for disaccharide conformation 2).

acetamido and O3 hydroxyl groups are displaced by 4.5 Å and 2.1 Å, respectively, approaching the opposite side of the binding pocket where residues Trp151 and Thr149 are located, and adopting a conformation close to that of the terminal ManNAc and GlcNAc residues from the trisaccharide ligand bound to SpaA_{SLH} (Fig. 3*B*).

Discussion

The crystal structures of wild-type and mutant SLH trimers from the *P. alvei* S-layer protein SpaA (SpaA_{SLH}) determined in the presence of the SCWP terminal monosaccharide analog reported earlier (27) demonstrated the remarkable conformational flexibility of the trimer while switching between the G2 and G1 SCWP binding sites and suggested a mechanism for relieving the strain encountered by S-layers during processes of cellular growth and division. The biological relevance of the binding site switch was demonstrated in that report (27) using synthetic, terminal pyruvylated ManNAc monosaccharide. To explore this observation, we now report the crystal structures

and binding characteristics of wild-type and mutant SpaA_{SLH} determined in the presence of the SCWP terminal di- and trisaccharide analogs (Fig. 1*B*).

Interestingly, compared with the nanomolar binding that wild-type SpaA_{SLH} achieved for the terminal SCWP monosaccharide (27), it showed now a slight decrease in binding affinity for the SCWP terminal disaccharide and a slight increase for the trisaccharide. Di- and trisaccharide analogs were observed to cocrystallize in G2 of wild-type SpaA_{SLH} (Fig. 2, *A* and *B*), while disaccharide was observed to cocrystallize in G1 of the conformationally rearranged SpaA_{SLH}/G109A single mutant (Fig. 2*C*) designed to destabilize binding in G2 (Table 1) and, again surprisingly, in G2 of the SpaA_{SLH}/G46A/G109A double mutant (Fig. 2*D*).

G2 of SpaA_{SLH} accommodates ligand flexibility at the penultimate SCWP sugar residue

In both the di- and trisaccharide-bound wild-type SpaA_{SLH} co-crystal structures, the terminal monosaccharide residue

forms contacts to the G2 site, with the remaining oligosaccharide residues extending into solvent where they form bridging contacts to the protein surface through a network of ordered water molecules (Fig. 3, *A* and *B*). Interestingly, the disaccharide bound to SpaA$_{SLH}$ is observed to adopt two distinct conformations (Conformations 1 and 2, Fig. 3*D*), while the bound trisaccharide is observed in a single conformation (Fig. 3*B*) corresponding to conformation 2 of the disaccharide, allowing the GlcNAc O3 to form a hydrogen bond with the Trp151 side chain nitrogen while the internal repeat ManNAc acetamido forms a 3.2 Å hydrogen bond (Fig. 3*B*) to the nitrogen atom of the GlcNAc acetamido. These conformational differences alone demonstrate that G2 accommodates significant flexibility in SCWP ligands by enabling the SCWP to pivot about the anchored terminal ManNAc.

It is interesting to compare the structure of SpaA$_{SLH}$ bound to the SCWP terminal disaccharide (4,6-Pyr-β-ᴅ-ManNAc-(1→4)-β-ᴅ-GlcNAcOMe) with the structure published from our groups of SpaA$_{SLH}$ bound to internal disaccharide (β-ᴅ-GlcNAc-(1→3)-4,6-Pyr-β-ᴅ-ManNAcOMe) (27), where the internal ManNAc residue is seen bound to the protein in largely the same manner as the terminal ManNAc residue. The lack of corresponding measurable binding in ITC experiments with the internal-repeat SCWP (27) indicates that this phenomenon is unlikely to represent a common biological interaction, but it does emphasize the flexibility of G2 as an adaptable primary SCWP-binding site.

Disaccharide in G1 of SpaA$_{SLH}$/G109A lies in an intermediate conformation

The deactivation of G2 using the G109A mutation forces SpaA$_{SLH}$ to utilize G1, which binds the longer, more biologically relevant SCWP terminal disaccharide ligand in a conformation intermediate between conformations 1 and 2 observed in G2 of wild-type SpaA$_{SLH}$. As observed for binding of the disaccharide in G2 of the SpaA$_{SLH}$ wild-type, only the terminal monosaccharide residue contacts the G1-binding site of the SpaA$_{SLH}$/G109A single-mutant (Fig. 1*D*), while the GlcNAc residue extends into solvent to form bridging contacts with the protein surface *via* an ordered network of water molecules (Fig. 3*C*).

Binding of the terminal SCWP monosaccharide in itself causes displacement of residues outside the monosaccharide receptor site required to accommodate longer SCWP oligosaccharides

Superposition of the monosaccharide receptor sites in the unliganded wild-type SpaA$_{SLH}$ and the corresponding disaccharide-bound forms shows that the binding of SCWP fragments longer than a monosaccharide in G2 in wild-type SpaA$_{SLH}$ and in G1 in SpaA$_{SLH}$/G109A requires displacement of a number of amino acid residues to avoid steric collision with internal saccharide residues. However, in a fascinating observation, the same relative displacements (27) are observed in the published structures of both proteins bound to monosaccharide. That is, the binding of the

monosaccharide alone is sufficient to cause rearrangement of the receptor-binding sites necessary to accommodate longer SCWP fragments.

In disaccharide-bound wild-type SpaA$_{SLH}$, the α-carbon atoms of residues SLH-30-31-32 (Lys110-Asp111-Leu112) that border the G2 monosaccharide receptor site and are adjacent to conserved residue SLH-Gly29 (Gly-109) are displaced by 1.0 Å, 1.1 Å, and 1.4 Å, respectively, relative to the SLH-30-31-32 α-carbon atoms in the unliganded structure (Fig. 4*A*). The monosaccharide acetamide moiety triggers this conformational shift first by displacing Leu112 away from the opening of G2. Together with the conserved Gly109 backbone flip, the Lys110 main chain atoms are forced toward the receptor site and stretch the Lys110 side chain atoms into near-full extension, which can accommodate the SCWP disaccharide GlcNAc residue (Fig. 4*B*).

A corresponding and somewhat more dramatic rearrangement occurs in G1 of the single mutant (Fig. 4*C*) through a slightly different mechanism. In the monosaccharide-bound G109A mutant, after compensating for the rearrangement that occurs during the conformational shift, the α-carbon atoms of G1 residues SLH-30-31-32 (Tyr47-Pro48-Gly49) are displaced by 4.6 Å, 6.4 Å, and 5.2 Å, respectively, relative to the unliganded structure (Fig. 4*C*). Specifically, monosaccharide binding directly displaces Pro48 as it stacks against the acetamido moiety, clearing the way for internal oligosaccharide residues (Fig. 4*D*) while concomitantly moving Tyr47 and Gly49. Similar changes are seen in the disaccharide-bound G109A mutant, where the rearrangements in G1 accommodate the corresponding terminal pyruvylated ManNAc residue and subsequent GlcNAc residue (Fig. 4*D*).

Binding affinity for G1 in SpaA$_{SLH}$/G109A is significantly weaker compared with G2 in the wild-type SpaA$_{SLH}$

SpaA$_{SLH}$ has three potential receptor sites, which complicates binding affinity determinations. Binding assays carried out by mutating the three SLH domain motifs TRAE (SLH1), TVEE (SLH2), and TRAQ (SLH3) respectively to TAAA reduced binding to 37%, 88%, and 50%, respectively (36, 37) relative to wild-type. Cocrystallization of wild-type SpaA$_{SLH}$ with a molar excess of SCWP fragments showed significant occupation of only the G2 site (27). Blackler *et al.* (27) explored the role of conserved residue SLH Gly-29 through sequential mutation to alanine and showed that by deactivating the G2 site through a G109A mutation, the protein underwent a conformational shift that enabled G1 to bind both the monosaccharide and internal disaccharide SCWP fragments, though with a significant reduction in affinity compared with wild-type (Table 1). When bound, G1 and G2 each make important contacts with the terminal, pyruvylated SCWP monosaccharide through residues SLH-Trp13, SLH Gly29, and SLH-Arg43. Yet the approximate geometries of the binding sites differ, including at residue positions SLH 30-31-32.

In unliganded SpaA$_{SLH}$, G1 adopts a slightly more "open" conformation (measuring 9.1 Å between Trp93 Cη2 and Gly46 O) than G2 (measuring 8.6 Å between Trp151 Cη2 and Gly109
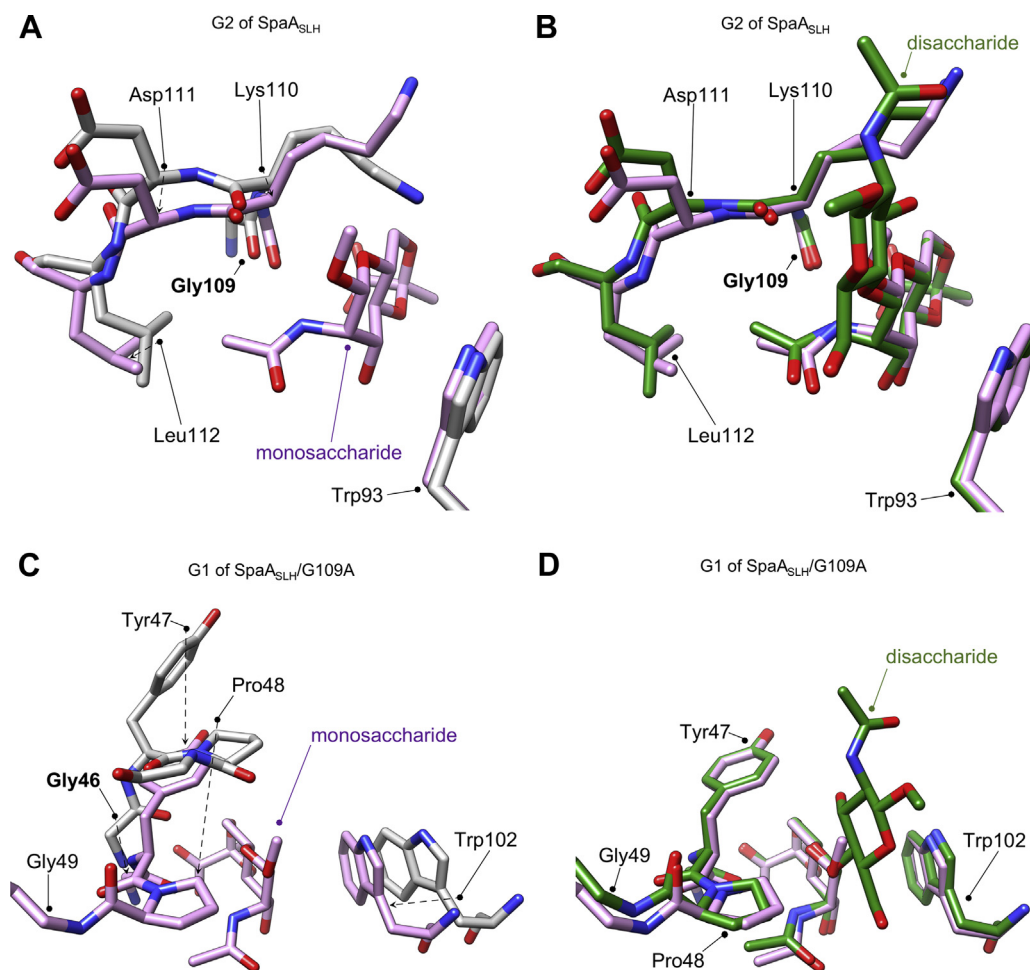
Figure 4. SpaA$_{SLH}$ residues SLH 30-31-32 that border the monosaccharide receptor site shift in response to terminal ManNAc binding to accommodate longer, more biologically relevant SCWP ligands. *A*, G2 of unliganded SpaA$_{SLH}$ (*grey*; PDB 6CWC) overlapped with G2 of monosaccharide-bound SpaA$_{SLH}$ (*purple*; PDB 6CWH) showing the relative displacement of these residues in G2 caused by binding of monosaccharide. *B*, the overlap of G2 of disaccharide-bound SpaA$_{SLH}$ (*green*) with G2 of monosaccharide-bound SpaA$_{SLH}$ (*purple*; PDB 6CWH) shows similar shifts, indicating that it is the binding of the monosaccharide, which is largely responsible for the shifts. *C*, G1 of unliganded SpaA$_{SLH}$ (*grey*) is overlapped with G1 of monosaccharide-bound SpaA$_{SLH}$/G109A single mutant (*purple*; PDB 6CWN) showing the relative displacement of these residues in G1 caused by binding of the monosaccharide. *D*, the overlap of G1 of disaccharide-bound SpaA$_{SLH}$/G109A (*green*) with G1 of monosaccharide-bound SpaA$_{SLH}$ (*purple*, PDB: 6CWN) shows similar shifts, indicating again that it is the binding of the monosaccharide, which is largely responsible for the shifts. All carbon atoms are colored according to the model descriptions above, with oxygen and nitrogen atoms colored in *red* and *blue*, respectively.

O). Ligand binding in either of G1 or G2 reduces the width of the receptor site to ∼7.5 Å, which means that G1—initially in a more open conformation prior to ligand binding—undergoes an additional 0.5 Å displacement to accommodate the SCWP interaction to adopt a geometry similar to that of G2-liganded SpaA$_{SLH}$. The binding of ligand in G2 does not significantly affect the open conformation of G1 observed in the completely unliganded stated.

The conformational change observed in the G109A mutant features displacement of the SLH2 domain toward SLH1 (27), as well as a >4.5 Å shift in G1 residues SLH 30-31-32 (Fig. 4, *C* and *D*). The latter SLH 30-31-32 movement occurs perpendicular to the SLH2 domain shift. The net result is a liganded G1 site with a strong resemblance to that of G2 (Fig. 4).

Collectively, the larger groove-narrowing and polypeptide loop shifts of G1 are consistent with the observed reduction in SpaA$_{SLH}$/G109A binding affinity ((27) and Table 1) relative to SpaA$_{SLH}$ wild-type.

"Doubly deactivated" SpaA$_{SLH}$/G46A/G109A mutant cocrystal structure accepts oligosaccharide ligand in G2

The introduction of a single G109A mutation in the G2 binding site of SpaA$_{SLH}$ was sufficient to shift all observed binding to the heretofore unoccupied G1 site. The simultaneous deactivation of both G1 and G2 by glycine to alanine mutations results in no observed binding by ITC (Table 1); however, consistent with the monosaccharide-bound SpaA$_{SLH}$/G46A/G109A structure, where binding in the crystalline environment is significantly enhanced compared with in solution (27), the crystal structure of the double mutant cocrystallized with approximate fivefold molar excess of disaccharide does show electron density in G2 corresponding to a fully occupied disaccharide SCWP fragment in Conformation 1 (Fig. 2D). In the presence of ligand in the crystal structure, the double mutant residues SLH 30-31-32 still undergo some displacement relative to the unliganded wild-type SpaA$_{SLH}$, even though the Gly109Ala deactivating mutation

prevents the G2 backbone flip, indicating the importance of the flip in the recognition and binding of the terminal monosaccharide.

SCWP binding in the SLH domains of Bacillus anthracis induces residue shifts similar to those observed in SpaA$_{SLH}$

Comparison of the published liganded (PDB: 6BT4 (29)) and unliganded (PDB: 3PYW (28)) *B. anthracis* Sap$_{SLH}$ structures reveals that G2 residues SHL 30-31-32 (Thr90-Gly91-Asn92) shift upon binding in a manner similar to that observed for *P. alvei* SpaA$_{SLH}$. This displacement is necessary to prevent steric collision with the bound oligosaccharide SCWP ligand. The Sap$_{SLH}$ binding site bears a strong structural similarity to that of SpaA$_{SLH}$, and the shifting Sap$_{SLH}$ residues, Thr90-Gly91-Asn92, are proximal to conserved residue SLH-Gly29. Both of these observations suggest that the triresidue shift, in addition to the conserved backbone flip mechanism, may be a common feature of the SCWP-SLH domain interaction. It is unclear whether the terminal SCWP residue alone is sufficient to induce these receptor site rearrangements as there are currently no published structures of monosaccharide-bound Sap$_{SLH}$; however, in *B. anthracis* (as in *P. alvei*), the penultimate SCWP residue, GlcNAc, lacks direct contacts with the protein, and the terminal monosaccharide predominates the SCWP-SLH domain binding interactions.

Experimental procedures

SpaA$_{SLH}$ protein production and purification

The SpaA$_{SLH}$ protein, consisting of amino acids 21 to 193 with a Ser-Gly-Ser linker followed by a C-terminal His$_6$ tag, and its single mutant (G109A) and double mutant (G46A/G109A) variants were produced and purified as described previously (27). Overexpression took place at 37 $^\circ$C with 200 rpm shaking and was induced *via* addition of IPTG to a final concentration of 0.6 mM once cells reached an OD$_{600}$ ∼0.6. Following induction, cells were incubated for a further 3 h before harvest by centrifugation at 6500g for 25 min. Cell pellets were resuspended in lysis buffer and lysed by sonication. The lysate was centrifuged at 10,000g, and the protein was purified from the supernatant using a combination of nickel NTA-affinity chromatography (Qiagen) and size exclusion chromatography (SEC), with a yield of ∼25 mg of each protein per liter of culture and a purity of >95% based on SDS-PAGE (38) analysis of the SEC fractions (27).

SpaA$_{SLH}$ isothermal titration calorimetry

ITC experiments were performed as described in (27) with minor modifications. The concentrations of the disaccharide and trisaccharide ligand are given by weight per volume (w/v). Protein concentrations were measured spectrophotometrically at 280 nm using a molar extinction coefficient of 18,450 M^{-1} cm^{-1}. For the ITC measurements with the disaccharide, a concentration of 500 μM was used for titration against SpaA$_{SLH}$ and SpaA$_{SLH}$/G109A at a concentration of 12.5 μM (protein-to-ligand ratio of 1:40). The trisaccharide was titrated

at a concentration of 340 μM against an 8.5-μM solution of SpaA$_{SLH}$ and at a concentration of 400 μM against a 10-μM solution of SpaA$_{SLH}$/G109A, respectively (protein-to-ligand ratio of 1:40). For the double mutant SpaA$_{SLH}$/G46A/G109A, a ratio of 1:50 was used (500 μM disaccharide to 10-μM solution of SpaA$_{SLH}$/G46A/G109A and 1000 μM trisaccharide to 20-μM solution of SpaA$_{SLH}$/G46A/G109A). The experiments were performed at least in triplicates.

SpaA$_{SLH}$ crystallization

Recombinant, purified wild-type SpaA$_{SLH}$, SpaA$_{SLH}$/G109A, and SpaA$_{SLH}$/G46A/G109A were concentrated using 3-kDa MWCO Amicon ultra centrifugal filter units and were cocrystallized with either 5 mM 4,6-Pyr-β-D-ManNAc-(1→4)-β-D-GlcNAcOMe disaccharide analog (35) or 1.1 mM 4,6-Pyr-β-D-ManNAc-(1→4)-β-D-GlcNAc-(1→3)-4,6-Pyr-β-D-ManNAcOMe trisaccharide analog (for the synthesis, see Supporting information; Figs. S3–S5; Schemes S1–S3). Screens were prepared using an Art Robbins Instruments crystal gryphon robot and Hampton 96-well Intelli plates. Cocrystals of SpaA$_{SLH}$ (15 mg/ml) and disaccharide were obtained within 1 week from Hampton Index screen condition number 2 (0.1 M sodium acetate trihydrate pH 4.5, 2.0 M ammonium sulphate). Cocrystals of SpaA$_{SLH}$/G109A (12 mg/ml) and disaccharide were obtained after 1 month from the Qiagen PEG II screen condition 15 (0.1 M HEPES pH 7.5, 25% (w/v) PEG 1000). Cocrystals of SpaA$_{SLH}$/G46A/G109A (19 mg/ml) and disaccharide were obtained after 1 week from the Qiagen PEG II screen condition 68 (0.1 M sodium acetate, 25% (w/v) PEG 4000, 8% (w/v) isopropanol). Cocrystals of SpaA$_{SLH}$ (18 mg/ml) and trisaccharide were obtained within 1 week from Qiagen JCSG+ screen condition number 83 (0.2 M Magnesium Chloride, 0.1 M Bis-Tris pH 5.5, 25% PEG 3350).

Data collection, structure solution, and refinement

Each crystal was resuspended in mother liquor containing 20% glycerol for 10 to 20 s prior to being flash-frozen at 100°K for data collection. For all structures, X-ray diffraction data were collected using a Dectris Pilatus 200 K detector coupled to a Rigaku Micromax-007 HF X-ray generator, and the data were scaled, averaged, and integrated using HKL2000. To generate a structure solution, molecular replacement was performed using Phaser from the CCP4 suite (34), with unliganded SpaA$_{SLH}$ (PDB: 6CWM) used as a search model for the SpaA$_{SLH}$ and SpaA$_{SLH}$/G46A/G109A structures, and SpaA$_{SLH}$/G109A (PDB: 6CWN, with the monosaccharide ligand removed) used as a search model for the SpaA$_{SLH}$/G109A structures. Following initial refinements, the 4,6-Pyr-β-D-ManNAc-(1→4)-β-D-GlcNAcOMe disaccharide and 4,6-Pyr-β-D-ManNAc-(1→4)-β-D-GlcNAc-(1→3)-4,6-Pyr-β-D-ManNAcOMe trisaccharide ligands were generated using the PRODRG2 Server and incorporated into their corresponding molecular models (39). All refinements and model building steps were performed using Coot (40) and Refmac5 from the CCP4 suite (34).

SASBMB

J. Biol. Chem. (2022) 298(4) 101745 **9**

Visualization and graphics

All figures depicting chemical structures or electron density were created using the UCSF Chimera Extensible Molecular Modeling System, developed by the Resource for Bio-computing, Visualization, and Informatics at the University of California, San Francisco, with support from NIH P41-GM103311 (41).

Data availability

The atomic coordinates and structure factors (7SV3, 7SV4, 7SV5, and 7SV6) have been deposited in the Protein Data Bank, Research Collaboratory for Structural Bioinformatics, Rutgers University, New Brunswick, NJ (http://www.rcsb.org/).

Abbreviations—The abbreviations used are: G1, groove 1 of SpaA_SLH; G2, groove 2 of SpaA_SLH; G3, groove 3 of SpaA_SLH; ITC, isothermal titration calorimetry; Sap_SLH, SLH domain trimer from the *Bacillus anthracis* S-layer protein Sap; S-layer, surface layer; SCWP, secondary cell wall polymer; SLH-domain, surface layer homology domain; SpaA_SLH, SLH domain trimer from the *Paenibacillus alvei* CCM 2051^T S-layer protein SpaA.

References

1. Engelhardt, H. (2007) Are S-layers exoskeletons? The basic function of protein surface layers revisited. *J. Struct. Biol.* **160**, 115–124
2. Sleytr, U. B., Egelseer, E. M., Ilk, N., Pum, D., and Schuster, B. (2007) S-layers as a basic building block in a molecular construction kit. *FEBS J.* **274**, 323–334
3. Sára, M., and Sleytr, U. B. (2000) S-layer proteins. *J. Bacteriol.* **182**, 859–868
4. Sleytr, U. B., Schuster, B., Egelseer, E. M., and Pum, D. (2014) S-layers: Principles and applications. *FEMS Microbiol. Rev.* **38**, 823–864
5. Sleytr, U. B., Messner, P., Pum, D., and Sára, M. (1993) Crystalline bacterial cell surface layers. *Mol. Microbiol.* **10**, 911–916
6. Messner, P., and Sleytr, U. B. (1992) Crystalline bacterial cell-surface layers. *Adv. Microb. Physiol.* **33**, 213–275
7. Bharat, T. A. M., von Kügelgen, A., and Alva, V. (2021) Molecular logic of prokaryotic surface layer structures. *Trends Microbiol.* **29**, 405–415
8. Hynönen, U., and Palva, A. (2013) *Lactobacillus* surface layer proteins: Structure, function and applications. *Appl. Microbiol. Biotechnol.* **97**, 5225–5243
9. Fagan, R. P., and Fairweather, N. F. (2014) Biogenesis and functions of bacterial S-layers. *Nat. Rev. Microbiol.* **12**, 211–222
10. Gerbino, E., Carasi, P., Mobili, P., Serradell, M. A., and Gomez-Zavaglia, A. (2015) Role of S-layer proteins in bacteria. *World J. Microbiol. Biotechnol.* **31**, 1877–1887
11. Schäffer, C., and Messner, P. (2017) Emerging facets of prokaryotic glycosylation. *FEMS Microbiol. Rev.* **41**, 49–91
12. Huber, C., Liu, J., Egelseer, E. M., Moll, D., Knoll, W., Sleytr, U. B., and Sára, M. (2006) Heterotetramers formed by an S-layer-streptavidin fusion protein and core-streptavidin as a nanoarrayed template for biochip development. *Small* **2**, 142–150
13. Sleytr, U. B., Huber, C., Ilk, N., Pum, D., Schuster, B., and Egelseer, E. M. (2007) S-layers as a tool kit for nanobiotechnological applications. *FEMS Microbiol. Lett.* **267**, 131–144
14. Sleytr, U. B., and Sára, M. (1997) Bacterial and archaeal S-layer proteins: Structure-function relationships and their biotechnological applications. *Trends Biotechnol.* **15**, 20–26
15. Schäffer, C., and Messner, P. (2004) Surface-layer glycoproteins: An example for the diversity of bacterial glycosylation with promising impacts on nanobiotechnology. *Glycobiology* **14**, 31R–42R
16. Schäffer, C., Novotny, R., Küpcü, S., Zayni, S., Scheberl, A., Friedmann, J., Sleytr, U. B., and Messner, P. (2007) Novel biocatalysts based on S-layer self-assembly of *Geobacillus stearothermophilus* NRS 2004/3a: A nano-biotechnological approach. *Small* **3**, 1549–1559
17. Völlenkle, C., Weigert, S., Ilk, N., Egelseer, E., Weber, V., Loth, F., Falkenhagen, D., Sleytr, U. B., and Sára, M. (2004) Construction of a functional S-layer fusion protein comprising an immunoglobulin G-binding domain for development of specific adsorbents for extracorporeal blood purification. *App Environ. Microbiol.* **70**, 1514–1521
18. Schuster, B. (2018) S-layer protein-based biosensors. *Biosensors (Basel)* **8**, 40
19. Walper, S. A., Anderson, G. P., Brozozog Lee, P. A., Glaven, R. H., Liu, J. L., Bernstein, R. D., Zabetakis, D., Johnson, L., Czarnecki, J. M., and Goldman, E. R. (2012) Rugged single domain antibody detection elements for *Bacillus anthracis* spores and vegetative cells. *PLoS One* **7**, e32801
20. Rodrigues-Oliveira, T., Belmok, A., Vasconcellos, D., Schuster, B., and Kyaw, C. M. (2017) Archaeal S-layers: Overview and current state of the art. *Front. Microbiol.* **8**, 2597
21. Albers, S.-V., and Meyer, B. H. (2011) The archaeal cell envelope. *Nat. Rev. Microbiol.* **9**, 414–426
22. Lupas, A., Engelhardt, H., Peters, J., Santarius, U., Volker, S., and Baumeister, W. (1994) Domain structure of the *Acetogenium kivui* surface layer revealed by electron crystallography and sequence analysis. *J. Bacteriol.* **176**, 1224–1233
23. Awram, P., and Smit, J. (2001) Identification of lipopolysaccharide O antigen synthesis genes required for attachment of the S-layer of *Caulobacter crescentus*. *Microbiology* **147**, 1451–1460
24. Engelhardt, H., and Peters, J. (1998) Structural research on surface layers: A focus on stability, surface layer homology domains, and surface layer-cell wall interactions. *J. Struct. Biol.* **124**, 276–302
25. Xu, Q., Resch, M. G., Podkaminer, K., Yang, S. H., Baker, J. O., Donohoe, B. S., Wilson, C., Klingeman, D. M., Olson, D. G., Decker, S. R., Giannone, R. J., Hettich, R. L., Brown, S. D., Lynd, L. R., Bayer, E. A., *et al.* (2016) Dramatic performance of *Clostridium thermocellum* explained by its wide range of cellulase modalities. *Sci. Adv.* **2**, e1501254
26. Usenik, A., Renko, M., Mihelic, M., Lindic, N., Borisek, J., Perdih, A., Pretnar, G., Muller, U., and Turk, D. (2017) The CWB2 cell wall-anchoring module is revealed by the crystal structures of the *Clostridium difficile* cell wall proteins Cwp8 and Cwp6. *Structure* **25**, 514–521
27. Blackler, R. J., Lopez-Guzman, A., Hager, F. F., Janesch, B., Martinz, G., Gagnon, S. M. L., Haji-Ghassemi, O., Kosma, P., Messner, P., Schäffer, C.,

and Evans, S. V. (2018) Structural basis of cell wall anchoring by SLH domains in *Paenibacillus alvei. Nat. Commun.* **9**, 3120

28. Kern, J., Wilton, R., Zhang, R., Binkowski, T. A., Joachimiak, A., and Schneewind, O. (2011) Structure of surface layer homology (SLH) domains from *Bacillus anthracis* surface array protein. *J. Biol. Chem.* **286**, 26042–26049

29. Sychantha, D., Chapman, R. N., Bamford, N. C., Boons, G. J., Howell, P. L., and Clarke, A. J. (2018) Molecular basis for the attachment of S-layer proteins to the cell wall of *Bacillus anthracis. Biochemistry* **57**, 1949–1953

30. Schäffer, C., Müller, N., Mandal, P. K., Christian, R., Zayni, S., and Messner, P. (2000) A pyrophosphate bridge links the pyruvate-containing secondary cell wall polymer of *Paenibacillus alvei* CCM 2051 to muramic acid. *Glycoconj J.* **17**, 681–690

31. Cava, F., de Pedro, M. A., Schwarz, H., Henne, A., and Berenguer, J. (2004) Binding to pyruvylated compounds as an ancestral mechanism to anchor the outer envelope in primitive bacteria. *Mol. Microbiol.* **52**, 677–690

32. Zarschler, K., Janesch, B., Pabst, M., Altmann, F., Messner, P., and Schäffer, C. (2010) Protein tyrosine *O*-glycosylation -a rather unexplored prokaryotic glycosylation system. *Glycobiology* **20**, 787–798

33. Mesnage, S., Fontaine, T., Mignot, T., Delepierre, M., Mock, M., and Fouet, A. (2000) Bacterial SLH domain proteins are non-covalently anchored to the cell surface *via* a conserved mechanism involving wall polysaccharide pyruvylation. *EMBO J.* **19**, 4473–4484

34. Winn, M. D., Ballard, C. C., Cowtan, K. D., Dodson, E. J., Emsley, P., Evans, P. R., Keegan, R. M., Krissinel, E. B., Leslie, A. G., McCoy, A., McNicholas, S. J., Murshudov, G. N., Pannu, N. S., Potterton, E. A., Powell, H. R., *et al.* (2011) Overview of the CCP4 suite and current developments. *Acta Crystallogr. D Biol. Crystallogr.* **67**, 235–242

35. Krauter, S., Schäffer, C., and Kosma, P. (2021) Synthesis of a pyruvylated N-acetyl-β-D-mannosamine containing disaccharide repeating unit of a cell wall glycopolymer from Paenibacillus alvei. *ARKIVOC* **4**, 137–151

36. Janesch, B., Messner, P., and Schäffer, C. (2013) Are the surface layer homology domains essential for cell surface display and glycosylation of the S-layer protein from *Paenibacillus alvei* CCM 2051^T? *J. Bacteriol.* **195**, 565–575

37. Zarschler, K., Janesch, B., Kainz, B., Ristl, R., Messner, P., and Schäffer, C. (2010) Cell surface display of chimeric glycoproteins *via* the S-layer of *Paenibacillus alvei. Carbohydr. Res.* **345**, 1422–1431

38. Laemmli, U. K. (1970) Cleavage of structural proteins during the assembly of the head of bacteriophage T4. *Nature* **227**, 680–685

39. Schüttelkopf, A. W., and van Aalten, D. M. (2004) PRODRG: A tool for high-throughput crystallography of protein-ligand complexes. *Acta Crystallogr. D Biol. Crystallogr.* **60**, 1355–1363

40. Emsley, P., Lohkamp, B., Scott, W. G., and Cowtan, K. (2010) Features and development of Coot. *Acta Crystallogr. D Biol. Crystallogr.* **66**, 486–501

41. Pettersen, E. F., Goddard, T. D., Huang, C. C., Couch, G. S., Greenblatt, D. M., Meng, E. C., and Ferrin, T. E. (2004) UCSF Chimera−a visualization system for exploratory research and analysis. *J. Comput. Chem.* **25**, 1605–1612